TU Delft

Delft University of Technology

Coupling biphasic homojunction interface and oxygen vacancies for enhanced polysulfide capture and catalytic conversion in Li-S batteries

Wang, Hao; Huang, Shidi; Cui, Zhe; Zhu, Jinqi; Zou, Rujia

DOI
10.1016/j.jechem.2025.04.062

Publication date
2025

Document Version
Final published version

Published in
Journal of Energy Chemistry

Citation (APA)
Wang, H., Huang, S., Cui, Z., Zhu, J., & Zou, R. (2025). Coupling biphasic homojunction interface and oxygen vacancies for enhanced polysulfide capture and catalytic conversion in Li-S batteries. *Journal of Energy Chemistry*, *108*, 485-494. https://doi.org/10.1016/j.jechem.2025.04.062

Important note
To cite this publication, please use the final published version (if applicable).
Please check the document version above.

Copyright
Other than for strictly personal use, it is not permitted to download, forward or distribute the text or part of it, without the consent of the author(s) and/or copyright holder(s), unless the work is under an open content license such as Creative Commons.

Takedown policy
Please contact us and provide details if you believe this document breaches copyrights.
We will remove access to the work immediately and investigate your claim.

This work is downloaded from Delft University of Technology.
For technical reasons the number of authors shown on this cover page is limited to a maximum of 10.

Green Open Access added to TU Delft Institutional Repository

'You share, we take care!' - Taverne project

https://www.openaccess.nl/en/you-share-we-take-care

Otherwise as indicated in the copyright section: the publisher is the copyright holder of this work and the author uses the Dutch legislation to make this work public.

Journal of Energy Chemistry 108 (2025) 485–494

Contents lists available at ScienceDirect

Journal of Energy Chemistry

journal homepage: www.elsevier.com/locate/jechem

http://www.journals.elsevier.com/journal-of-energy-chemistry/

Coupling biphasic homojunction interface and oxygen vacancies for enhanced polysulfide capture and catalytic conversion in Li-S batteries

Hao Wang [a,b], Shidi Huang [c,*], Zhe Cui [b,d], Jinqi Zhu [b], Rujia Zou [b,*]

[a] Department of Radiation Science and Technology, Faculty of Applied Sciences, Delft University of Technology, Mekelweg 15, Delft 2629JB, the Netherlands
[b] State Key Laboratory of Advanced Fiber Materials, College of Materials Science and Engineering, Donghua University, Shanghai 201620, China
[c] School of Ecological Technology and Engineering, Shanghai Institute of Technology, Shanghai 201418, China
[d] Macao Institute of Materials Science and Engineering (MIMSE), Faculty of Innovation Engineering, Macau University of Science and Technology, Taipa, Macao 999078, China

ARTICLE INFO

Article history:
Received 28 March 2025
Revised 25 April 2025
Accepted 26 April 2025
Available online 2 May 2025

Keywords:
Li-S batteries
Biphasic homojunctions
Polysulfides adsorption and conversion
TiO_2

ABSTRACT

Lithium-sulfur (Li-S) batteries promise high energy density but suffer from low conductivity, polysulfide shuttling, and sluggish conversion kinetics. The construction of heterointerfaces is an effective strategy for enhancing both polysulfide adsorption and conversion; however, the poor lattice compatibility in the heterointerface formed by different materials hinders interfacial charge transfer. In response to these challenges, herein, a biphasic homojunction of TiO_2 enriched with oxygen vacancies and decorated with nitrogen-doped carbon nanotubes (B-TiO_{2-x}@NCNT) was designed to simultaneously enhance adsorption ability and catalytic activity. This homojunction interface composed of rutile (1 1 0) and anatase (1 0 1) plane exhibits excellent compatibility, and density functional theory (DFT) calculations reveal that this biphasic interface possesses a much higher binding energy to polysulfides compared to single-phase TiO_2. Additionally, NCNTs are in situ grown on both interior and exterior surfaces of the hollow TiO_2 nanospheres, facilitating rapid electron transfer for the encapsulated sulfur. The homojunction interface synergistically leverages the oxygen vacancies and highly conductive NCNTs to enhance the bidirectional catalytic activity for polysulfide conversion. Therefore, in this multifunctional sulfur-host, polysulfides are first strongly adsorbed at the homojunction interfaces and subsequently undergo smooth conversion, nucleation, and decomposition, completing a rapid sulfur redox cycle. The assembled Li-S battery delivered a high specific capacity of 1234.3 mAh g^{-1} at 0.2 C, long cycling stability for over 1000 cycles at 5 C with a low decay rate of 0.035%, and exciting areal capacity at a high sulfur loading of 5.6 mg cm^{-2} for 200 cycles.

© 2025 Science Press and Dalian Institute of Chemical Physics, Chinese Academy of Sciences. Published by Elsevier B.V. and Science Press. All rights are reserved, including those for text and data mining, AI training, and similar technologies.

1. Introduction

Lithium-sulfur (Li-S) batteries rely on the conversion reaction of sulfur cathode, which therefore provides a theoretical energy density of 2600 Wh kg^{-1} far exceeding that of insertion reactions of layered oxide cathodes [1,2]. Furthermore, sulfur is one of the most abundant elements in the Earth's crust, which is economically viable and environmentally friendly, making Li-S battery a promising candidate to meet the sustainable development of modern society [3]. However, the practical application of Li-S battery is hindered by several challenges, such as the intrinsic insulating nature of sulfur and its discharge products (Li_2S_2/Li_2S), the severe shuttle effect caused by the high solubility of polysulfides in liquid electrolytes [4], high volume changes during cycling, and the sluggish reaction kinetics of sulfur reduction and Li_2S_2/Li_2S oxidation [5]. These issues result in low practical capacity, poor Coulombic efficiency, and undesirable cycling life [6].

The enhancement of the conductivity of sulfur-host and its adsorption ability to polysulfides, along with the improvement of catalytic activity for polysulfides conversion, represents the key strategy to address the above-mentioned challenges [7]. Carbon matrices are usually applied to improve the conductivity of sulfur cathode [8,9], and polar materials such as transition metal oxides are widely investigated due to their (electro)chemical stability and high binding energies with liquid polysulfides [10–13]. The polysulfides formed during electrochemical reactions are more likely to be absorbed on the surface of oxides rather than shuttling due to their much higher adsorption ability compared to

* Corresponding authors.
E-mail addresses: sdhuang@sit.edu.cn (S. Huang), rjzou@dhu.edu.cn (R. Zou).

https://doi.org/10.1016/j.jechem.2025.04.062
2095-4956/© 2025 Science Press and Dalian Institute of Chemical Physics, Chinese Academy of Sciences. Published by Elsevier B.V. and Science Press. All rights are reserved, including those for text and data mining, AI training, and similar technologies.

1,3-dioxolane (DOL) and 1,2-dimethylethane (DME) [14]. Despite these advantages, oxides exhibit low conductivity and no or poor catalytic capability for the conversion of sulfur species, which results in slow reaction kinetics and low utilization of active materials. Oxygen vacancy engineering can modify the electron band structure of metal oxides, which can enhance the surface electron transfer [15]. Nevertheless, the construction of oxygen vacancies has a limited effect on improving the adsorption ability to polysulfides. One theoretical study even reported that the adsorption energy of Li_2S_8 on TiO_{2-x} (1 1 0) surface is –3.14 eV, even a bit lower than that without oxygen vacancies (–3.71 eV) [16].

Additionally, the deliberate design of interfacial chemistry alters the electronic structure by integrating oxide with another compound, thereby generating distinct properties that differ from those of either individual component. This approach often plays a crucial role in enhancing the electrocatalytic performance in Li-S batteries [17]. Ren et al. reported a core-shell VP-VO heterostructure, which demonstrated a balanced adsorption and catalytic effect for a high-energy-density Li-S pouch cell [18]. The effective but moderate adsorption of polysulfides not only mitigates the shuttle effect but also facilitates the subsequent polysulfide conversion process [18]. Meanwhile, strong catalytic activity improves the electrochemical reaction kinetics and helps reduce polysulfide accumulation, thereby boosting the cycling stability of Li-S battery [19,20]. Similarly, twin-born TiO_2-TiN heterostructure and in situ crafted TiO_2-MXene were investigated and contributed to the smooth trapping-diffusion-conversion of polysulfides [21,22]. However, among all these heterostructures, the disparate properties and poor lattice matching of two distinct materials result in poor interfacial contact, which also leads to interface separation and slow charge transfer at the heterostructure interface [23,24]. A key challenge in interfacial chemistry is how to simultaneously improve the adsorption and catalytic performance of oxide-based sulfur-host materials, while maintaining the compatibility and stability of the interface [25,26]. In light of this, homojunctions composed of different phases have been proven to exhibit better interfacial contact and enhanced catalytic performance due to almost perfect lattice matching [26,27]. So far, the research of the fundamental mechanisms governing polysulfide adsorption and catalytic effect at homojunction interface remains limited and inadequately understood, highlighting a critical gap in current research.

Herein, a biphasic homojunction interface, consisting of the TiO_2 anatase (1 0 1) plane and rutile (1 1 0) plane, has been successfully synthesized as a representative material. Theoretical calculations were first performed and revealed that the biphasic homojunction interface between anatase TiO_2 (A-TiO_2) and rutile TiO_2 (R-TiO_2) exhibited much higher binding energies to polysulfides compared to any single phases (Scheme 1). Polysulfides are strongly adsorbed at the biphasic interface and the shuttle effect is effectively addressed. To further improve the conductivity, this biphasic TiO_2 is enriched with oxygen vacancies and decorated with nitrogen-doped carbon nanotubes (B-TiO_{2-x}@NCNT). Additionally, NCNTs were in situ grafted in both the interior and exterior of the TiO_2, providing additional channels for the rapid diffusion of electrons and Li^+ to sulfur encapsulated within the TiO_2, thereby enhancing the redox kinetics of Li-S electrochemistry. Li_2S precipitation and decomposition experiments have demonstrated the excellent bidirectional catalytic effect on both nucleation and oxidation of Li_2S, leading to improved Coulombic efficiency and high utilization of active materials. Benefiting from the above advantages, this Li-S battery delivers encouraging electrochemical performance, including outstanding long cycling stability for 1000 cycles at 5 C with a low decay rate of 0.035% and superior areal capacity at high sulfur loading of 5.4 mg cm^{-2}.

2. Results and discussion

The schematic synthesis process of TiO_2-based sulfur hosts in this study is illustrated in Fig. 1(a). First, melamine formaldehyde (MF) spheres (Fig. S1a) are synthesized as sacrificial templates to create the hollow structure. Subsequently, the scanning electron microscope (SEM) images show clearly that a Ti-containing layer with a thickness of 25–30 nm is coated on MF spheres to form MF@T spheres (Fig. S1b and d), followed by another Ni-containing layer to form MF@T@N spheres (Fig. S1c, e, and f) and the thickness of outer layer increased to 40 nm. Finally, MF@T is annealed in air at 650 °C to prepare TiO_2 hollow nanospheres with single rutile phase (R-TiO_2) as shown in Fig. 1(b). The rutile TiO_2 hollow nanospheres with abundant oxygen vacancies and

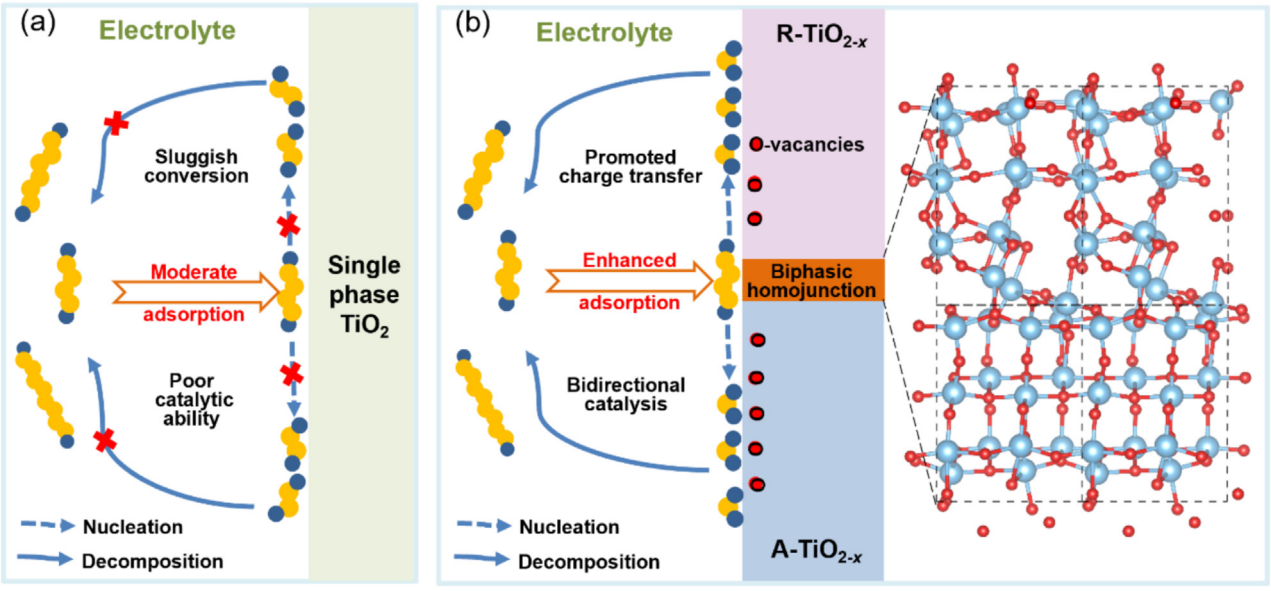

Scheme 1. The schematic illustration of adsorption and conversion for polysulfides on (a) a single-phase TiO_2 without oxygen vacancies and (b) oxygen vacancy-rich TiO_2 with the biphasic homojunction composed of anatase and rutile TiO_2.

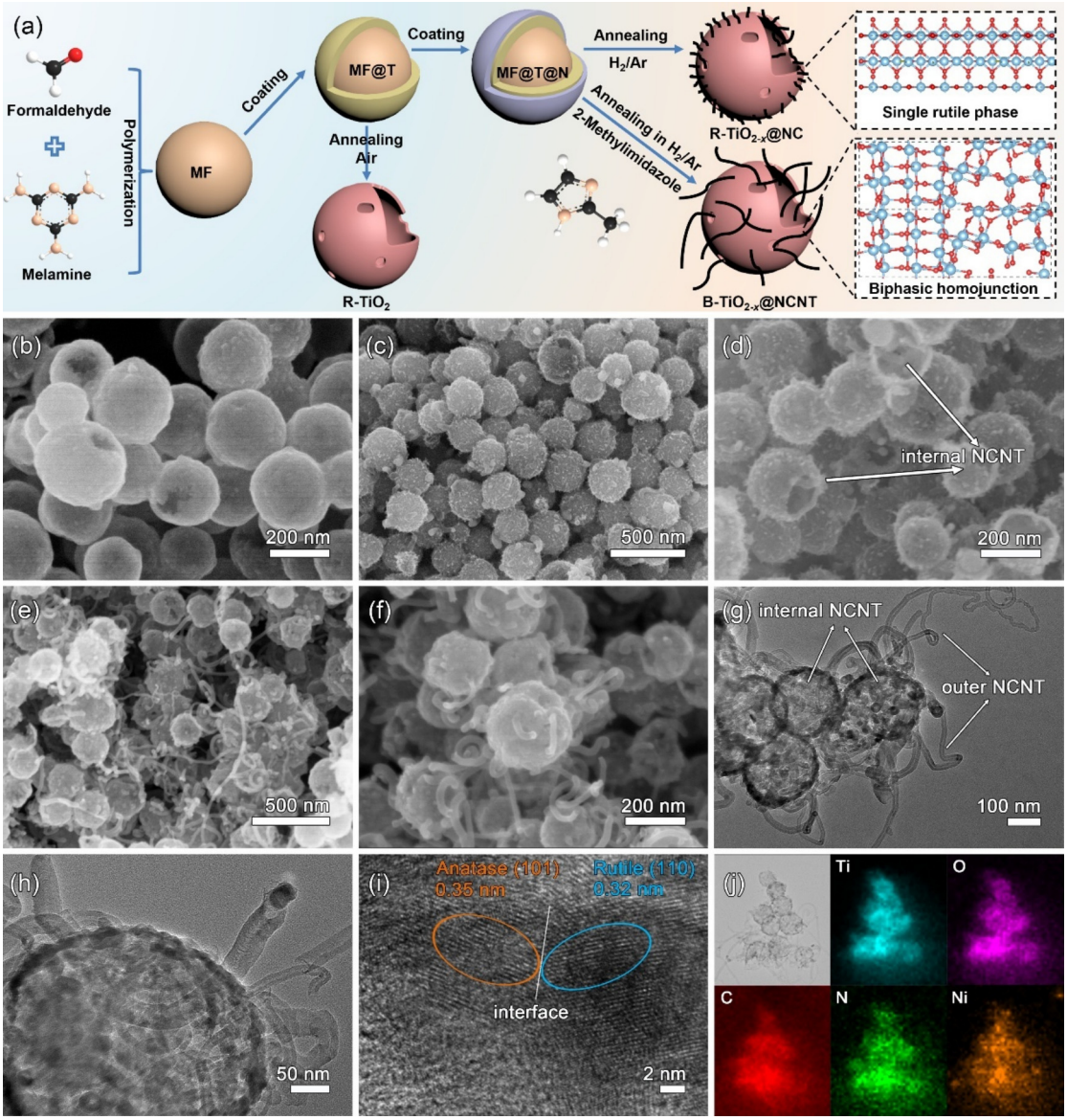

Fig. 1. (a) Schematic illustration of the synthesis process for sulfur hosts of B-TiO_{2-x}@NCNT, R-TiO_{2-x}@NC, and R-TiO_2. SEM images of (b) R-TiO_2, (c, d) R-TiO_{2-x}@NC, and (e, f) B-TiO_{2-x}@NCNT. (g, h) TEM images, (i) HRTEM image, and (j) EDS mapping of Ti, O, C, N, and Ni elements from B-TiO_{2-x}@NCNT.

nitrogen-doped carbon (R-TiO_{2-x}@NC) are obtained by annealing MF@T@N under the same conditions except for the reductive atmosphere of H_2/Ar. The surface morphology of R-TiO_{2-x}@NC is very rough (Fig. 1c) because some short NCNTs are formed on the surface of R-TiO_{2-x}@NC due to the partial carbonization of the MF template at high temperature. Additionally, since the carbon-containing gas diffuses from inside out, NCNTs could be grown inside of R-TiO_{2-x}@NC, which can be further confirmed from the broken R-TiO_{2-x}@NC spheres (Fig. 1d). These short NCNTs could also improve the electronic conductivity of TiO_2, but only in a small and localized area, which could not bridge all separate R-TiO_{2-x}@NC spheres. To further increase the length of NCNTs to link all TiO_2 spheres together, additional 2-methylimidazole was introduced as carbon and nitrogen source, resulting in the in-situ growth of long NCNTs both inside and outside of TiO_2 hollow spheres. As shown in Fig. 1(e and f), the NCNT is significantly longer and links the TiO_2 spheres together. There is a small and dark particle embedded in the top of every NCNT, which is determined to be Ni nanoparticles according to the catalytic growth mechanism of NCNT [28]. Additionally, the addition of 2-methylimidazole during the annealing process will also result in a mixed anatase and rutile phase of TiO_2, which will be discussed further in the next section. In Fig. 1(g and h), the transmission electron microscope (TEM) images show clearly that there are also a large number of NCNTs inside of the hollow TiO_2 sphere, which would greatly enhance the electronic conductivity after mixing with sulfur. What is more, the escape of high-pressure gas generated inside at high temperature causes the formation of pores on the surface of B-TiO_{2-x}@NCNT, R-TiO_{2-x}@NC, and R-TiO_2. These pores provide channels for molten sulfur and electrolytes to enter the inside of the hollow structure. The high-resolution TEM (HRTEM) image in Fig. 1(i) indicates that B-TiO_{2-x}@NCNT consists of the rutile phase and anatase phase, and the biphasic homojunction interface between the rutile phase and anatase phase is clearly visible. A lattice spacing of approximately 0.35 nm is attributed to the (1 0 1) plane of anatase TiO_2, while another lattice spacing of 0.32 nm is for the (1 1 0) plane of rutile TiO_2 [23,29]. The homojunction interface between anatase and rutile TiO_2 will regenerate the

electric field, which is expected to enhance interactions with lithium polysulfides in Li-S electrochemistry [30,31]. Energy dispersive spectrometer (EDS) mapping in Fig. 1(j) shows the elemental distribution of Ti, O, C, N, and Ni. The Ti and O elements are concentrated within the B-TiO_{2-x}@NCNT structure, while C, N, and Ni are more diffusely distributed outside of TiO_2 spheres. The elemental distribution is consistent with the B-TiO_{2-x}@NCNT microstructure observed in SEM and TEM images.

The crystalline structures of B-TiO_{2-x}@NCNT, R-TiO_{2-x}@NC, and R-TiO_2 are investigated by X-ray diffraction (XRD) technique (Fig. 2a). XRD patterns of R-TiO_2 and R-TiO_{2-x}@NC are almost identical, with main characteristic peaks observed at 27.4°, 36.1°, 41.2°, and 54.3°, corresponding to the (1 1 0), (1 0 1), (1 1 1), and (2 1 1) planes of rutile TiO_2 (PDF#99-0090), respectively [32]. In addition to the rutile phase, B-TiO_{2-x}@NCNT also exhibits clear characteristic peaks at 25.3°, 37.8°, and 48.0°, which belong to (1 0 1), (0 0 4), and (2 0 0) planes of anatase TiO_2 (PDF#99-0008) [33]. This indicates that the TiO_2 in B-TiO_{2-x}@NCNT is a mixture of anatase and rutile phase, whereas the R-TiO_2 and R-TiO_{2-x}@NC are predominantly composed of a single rutile phase. The rutile phase of TiO_2 exhibits higher thermodynamic stability, while the anatase phase of TiO_2 is a metastable phase that typically undergoes irreversible transformation to the rutile phase at high temperatures [34]. Interestingly, despite being synthesized at the same temperature as R-TiO_2 and R-TiO_{2-x}@NC, the B-TiO_{2-x}@NCNT contains a significant amount of anatase phase. This is attributed to the addition of a large quantity of reductive 2-methylimidazole as a carbon source to synthesize NCNT. The high reductivity during high-temperature annealing process leads to instability in the nucleation and growth of TiO_2. In other words, the formation of the anatase phase occurs alongside the growth of long NCNTs, and it is not possible to maintain a pure rutile phase through annealing at 650 °C. Additionally, numerous theoretical and experimental studies have demonstrated that the anatase TiO_2 exhibits higher catalytic activity compared to the rutile phase [35–37]. Here, the anatase TiO_2 is also expected to enhance the catalytic activity for the conversion of lithium polysulfides.

The electron paramagnetic resonance (EPR) technique is exploited to confirm the presence of oxygen vacancies in TiO_2 after being treated in H_2/Ar. As shown in Fig. 2(b), a very strong resonance signal at a *g*-value of 2.003 is observed in B-TiO_{2-x}@NCNT [38], the intensity of which is slightly higher than that of R-TiO_{2-x}@NC and much higher than that of R-TiO_2, indicating the presence of a large number of oxygen vacancies in B-TiO_{2-x}@NCNT. The oxygen vacancies would alter the valence electron distribution of TiO_2, shift the conduction band toward the Fermi level, and boost the conductivity [16]. Moreover, the presence of oxygen vacancies provides a lot of active sites on the surface of TiO_2 that facilitate the rapid conversion of absorbed polysulfides [23]. It should be mentioned here that even in R-TiO_2, there is also a very low oxygen vacancy signal due to the reducing gas from sacrificial MF templates. However, the intensity of oxygen vacancies in R-TiO_2 is much lower compared to annealing in H_2/Ar. Thermogravimetric analysis (TGA) was conducted to investigate the carbon content of as-synthesized materials (Fig. 2c). Taking R-TiO_2 as a baseline, which is completely carbon-free, the loss in weight of R-TiO_{2-x}@NC and B-TiO_{2-x}@NCNT between 300 and 600 °C in air can be assigned to the combustion of carbon. This enables determining that the NCNT content in B-TiO_{2-x}@NCNT is as high as 50.1 wt%, which would greatly enhance the conductivity of this sulfur host.

X-ray photoelectron spectroscopy (XPS) is further performed to analyze the composition and chemical bonds of B-TiO_{2-x}@NCNT, R-TiO_{2-x}@NC, and R-TiO_2. The XPS survey spectra in Fig. S2 reveal that the R-TiO_2 primarily consists of Ti and O elements, with only a small amount of carbon, which is likely due to surface adsorption. In addition to the typical Ti and O, the R-TiO_{2-x}@NC also contains small amounts of C and N elements from the partial carbonization of template MF spheres. In contrast, the XPS survey of B-TiO_{2-x}@NCNT exhibits large amounts of C and N elements attributed to a large amount of in-situ grown NCNTs. Fig. 2(d) presents the high-resolution XPS spectra of Ti 2*p* for B-TiO_{2-x}@NCNT, R-TiO_{2-x}@NC, and R-TiO_2. All spectra display a pair of Ti–O peaks around ~465 eV (Ti $2p_{1/2}$) and ~461 eV (Ti $2p_{3/2}$) [39]. Additionally, the lack of oxygen in TiO_2 alters the bonding of cations and anions, causing the binding energies of Ti–O peaks to shift to lower values as shown in Fig. 2(d). Based on this lower shift, it can be further inferred that the concentration of oxygen vacancies increases from R-TiO_2 to R-TiO_{2-x}@NC and then to B-TiO_{2-x}@NCNT, which aligns with EPR observations [40,41]. This further demonstrates that the concentration of oxygen vacancies is in agreement with the EPR measurements. Fig. 2(e) displays the C 1*s* spectra, and both

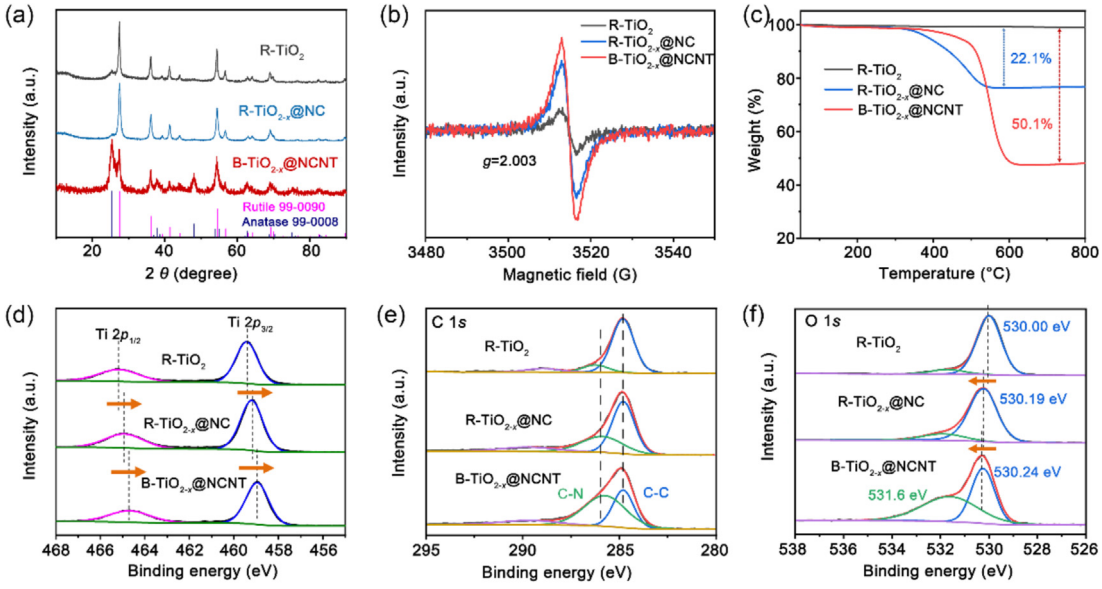

Fig. 2. (a) XRD patterns, (b) EPR curves, and (c) TGA measurements of R-TiO_2, R-TiO_{2-x}@NC, and B-TiO_{2-x}@NCNT. The high-resolution XPS of (d) Ti 2*p*, (e) C 1*s*, and (f) O 1*s* for R-TiO_2, R-TiO_{2-x}@NC, and B-TiO_{2-x}@NCNT.

B-TiO_{2-x}@NCNT and R-TiO_{2-x}@NC show obvious C–N bonds at 285.8 eV besides the C–C bonds at 284.8 eV [42], which also confirms the successful doping of nitrogen in carbon. Nitrogen doping can not only enhance the conductivity of carbon nanotubes but also increase their surface polarity, thereby improving the polar-polar adsorption to polysulfides [43,44]. In Fig. 2(f), the O 1*s* signal shows that the main peak for R-TiO_2 is located at 530.00 eV, corresponding to the O–Ti bond [45]. In comparison to R-TiO_2, the O–Ti peaks of R-TiO_{2-x}@NC and B-TiO_{2-x}@NCNT show a slightly positive shift to 530.19 and 530.24 eV, respectively, which is attributed to the increased number of oxygen vacancies [46]. Moreover, B-TiO_{2-x}@NCNT exhibits an obvious additional peak of the O–C bond at 531.6 eV [47]. The increased intensity of the O–C bond in B-TiO_{2-x}@NCNT is attributable to its higher carbon content.

Anatase and rutile TiO_2 both belong to the tetragonal crystal system but exhibit different dominant exposed facets due to their distinct crystallographic arrangements and surface energies. For the anatase TiO_2 (space group $I4_1/amd$), the (1 0 1) plane is the most thermodynamically stable surface, owing to its low surface energy and the minimum number of unsaturated atoms. Similarly, the rutile TiO_2 (space group $P4_2/mnm$) typically exposes the (1 1 0) facet, which is the most stable and frequently observed surface during crystal growth [48,49]. This is also consistent with HRTEM observations (Fig. 1i), which confirmed the presence of a biphasic homojunction interface between the anatase (1 0 1) plane and the rutile (1 1 0) plane. These facets not only dominate the morphology of TiO_2 nanocrystals but also significantly influence their adsorption toward lithium polysulfides. The shuttle effect poses one of the greatest challenges to the cycling stability of Li-S batteries, while enhancing the adsorption ability of sulfur-host materials to polysulfides is crucial for mitigating the shuttle effect. The contact area of this biphasic interface will regenerate the electron distribution, which will also affect the adsorption ability to lithium polysulfides accordingly [30,31]. To have a deep understanding of the adsorption behavior to polysulfides at the homojunction interface, density functional theory (DFT) calculations are first performed. Fig. 3(a) and Figs. S3 and S4 illustrate the optimized interaction with various polysulfides of the biphasic TiO_2 (B-TiO_2) between anatase (1 0 1) plane and rutile (1 1 0) plane, single anatase (1 0 1) plane (A-TiO_2), and single rutile (1 1 0) plane (R-TiO_2). From the interaction structures, it can be inferred that TiO_2 with all different phases immobilizes lithium polysulfides by forming Ti–S and O–Li bonds. However, the binding energies of Li_2S_8, Li_2S_6, Li_2S_4, Li_2S_2, and Li_2S on the biphasic homojunction are calculated to be −6.54, −7.22, −7.07, −6.29, and −7.78 eV, respectively, which are much higher than that of both anatase and rutile TiO_2. DFT calculations predict that B-TiO_{2-x}@NCNT theoretically has stronger adsorption energies compared to R-TiO_2 and R-TiO_{2-x}@NC with single rutile phase, particularly for long-chain polysulfides (Li_2S_x, $4 \le x \le 8$). For example, as shown in Fig. 3(b), the binding energies at the biphasic interface to Li_2S_8 and Li_2S_6 are 1.64 and 2.23 times than those on single rutile surface, respectively. Long-chain polysulfides possess a more severe shuttle effect than short-chain polysulfides (Li_2S_x, $2 < x < 4$) due to their higher solubility in liquid electrolytes, leading to a more severe shuttle effect. The strong adsorption ability of B-TiO_{2-x}@NCNT holds significant potential for effectively mitigating the occurrence of shuttling phenomenon.

To present a more straightforward observation of the adsorption ability of B-TiO_{2-x}@NCNT, R-TiO_{2-x}@NC, and R-TiO_2 to polysulfides, a visual adsorption experiment was conducted as shown in Fig. 3(c). Equal amounts of B-TiO_{2-x}@NCNT, R-TiO_{2-x}@NC, and R-TiO_2 were added in electrolytes with Li_2S_4 and labeled as solution 1, 2, and 3, respectively. Initially, the solution 1 and 2 appeared slightly darker due to the black color of B-TiO_{2-x}@NCNT and R-TiO_{2-x}@NC. After setting for 24 h, the solutions containing B-TiO_{2-x}@NCNT (solution 1) became colorless, while solution 3 still exhibited in yellow color. The visual adsorption experiment demonstrates that B-TiO_{2-x}@NCNT can adsorb Li_2S_4 effectively, whereas R-TiO_2 exhibits poor adsorption ability. The strong adsorption ability of B-TiO_{2-x}@NCNT arises not only from the chemical binding of the biphasic homojunction interface but also from the physical interactions with NCNTs. As shown in Fig. 3(d),

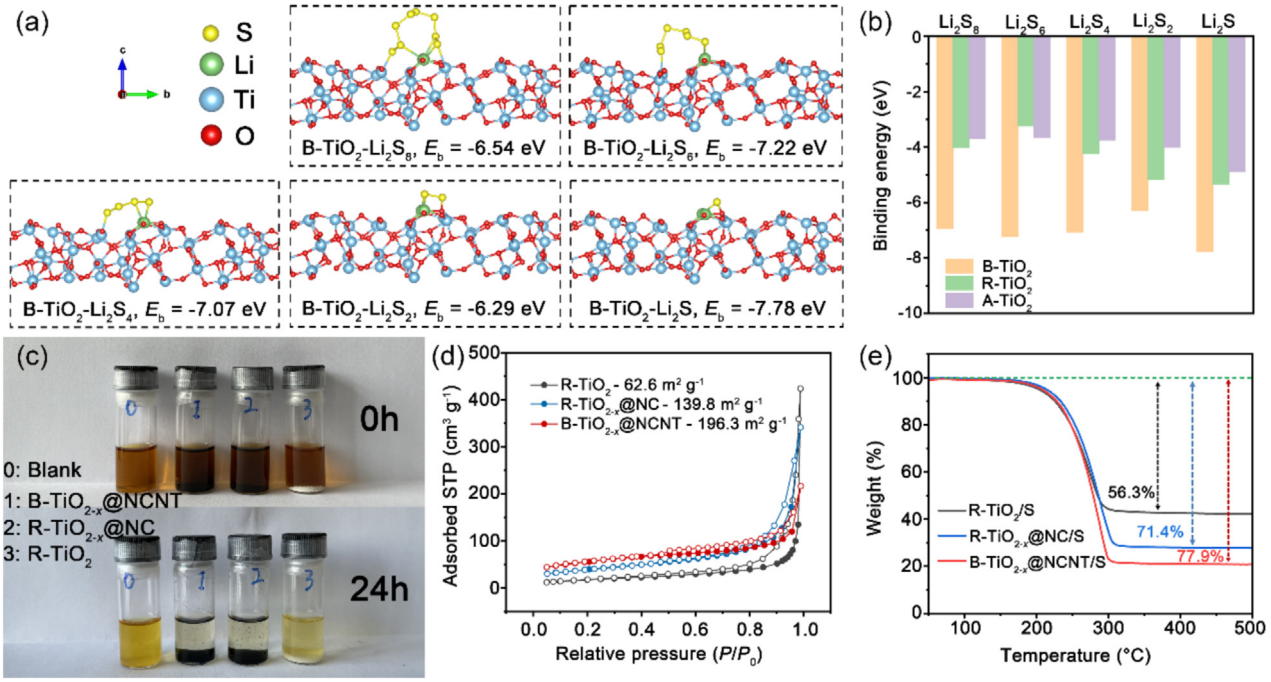

Fig. 3. (a) The optimized interaction configurations of biphasic homojunction between anatase (1 0 1) plane and rutile (1 1 0) plane (B-TiO_2) to different orders polysulfides (Li_2S_8, Li_2S_6, Li_2S_4, Li_2S_2, and Li_2S). (b) Comparison of calculated adsorption energies of B-TiO_2, R-TiO_2, and A-TiO_2 to different orders polysulfides (Li_2S_8, Li_2S_6, Li_2S_4, Li_2S_2, and Li_2S). (c) Optical photographs of pure Li_2S_4 solution (0), and with 10 mg B-TiO_{2-x}@NCNT (1), R-TiO_{2-x}@NC (2), and R-TiO_2 (3) at 0 and 24 h. (d) Nitrogen adsorption-desorption isotherms of R-TiO_2, R-TiO_{2-x}@NC, and B-TiO_{2-x}@NCNT. (e) TGA curves of R-TiO_2/S, R-TiO_{2-x}@NC/S, and B-TiO_{2-x}@NCNT/S under N_2 atmosphere.

B-TiO_{2-x}@NCNT shows the largest specific surface area due to the abundant NCNTs, reaching up to 196.3 m^2 g^{-1}. R-TiO_{2-x}@NC follows with a specific surface area of 139.8 m^2 g^{-1}, while R-TiO_2 shows the smallest surface area of 62.6 m^2 g^{-1}. What is more, the nitrogen doping in carbon nanotubes increases the electron density and modifies the charge distribution symmetry in pure carbon [50], which can enhance surface polarity and improve the interactions with polysulfides [43]. The above theoretical calculations and experimental results confirm that B-TiO_{2-x}@NCNT could effectively address the shuttle effect through the combination of strong chemical binding from the biphasic interface and enhanced physical immobilization from a larger specific surface area.

The morphology of B-TiO_{2-x}@NCNT after mixing with sulfur by melt-diffusion method is shown in Fig. S5 [51]. The surface exhibits a thin layer of amorphous material, attributed to the molten sulfur, without noticeable agglomeration or large sulfur particles. The B-TiO_{2-x}@NCNT framework retains its original morphology, indicating uniform sulfur dispersion throughout the composite. Moreover, TGA is conducted to investigate the sulfur content of B-TiO_{2-x}@NCNT, R-TiO_{2-x}@NC, and R-TiO_2. As shown in Fig. 3(e), the weight loss between 200 and 300 °C under N_2 atmosphere corresponds to the amount of sulfur, which can be inferred that the sulfur content in B-TiO_{2-x}@NCNT/S, R-TiO_{2-x}@NC/S, and R-TiO_2/S is 77.9, 71.4, and 56.3 wt%, equivalent to a sulfur loss of 11.9, 37.6, and 67.9 wt% during molten-diffusion process, respectively. The loss of sulfur is attributed to sublimation during the heating process. The sulfur-host B-TiO_{2-x}@NCNT presents the lowest sulfur loss due to its better affinity to sulfur and larger surface area, which collectively enable B-TiO_{2-x}@NCNT/S to achieve a high sulfur loading. Due to the high content of sulfur, the XRD patterns of B-TiO_{2-x}@NCNT/S mainly exhibit the characteristic peaks of sulfur (Fig. S6). A high sulfur loading is a key factor in achieving high-energy-density Li-S batteries to meet the practical application requirements in the future.

To investigate the electrochemical redox reaction and conversion process of lithium polysulfides, symmetric cells were assembled by B-TiO_{2-x}@NCNT, R-TiO_{2-x}@NC, and R-TiO_2 as electrodes, respectively. The electrolyte consisted of 0.1 M Li_2S_6 and 1 M LiTFSI in DOL/DME with a volume ratio of 1:1. As shown in Fig. 4(a–c), there are no redox peaks in the cyclic voltammetry (CV) curves without Li_2S_6, indicating that the DOL/DME and LiTFSI are electrochemically stable within this voltage window and do not contribute to the current density. Symmetric peaks occur in the CV scan with Li_2S_6, corresponding to the redox reactions of Li_2S_6 on the surface of B-TiO_{2-x}@NCNT, R-TiO_{2-x}@NC, and R-TiO_2 electrodes. Taking the negative scan as an example, several reduction peaks are observed for B-TiO_{2-x}@NCNT (Fig. 4a), corresponding to stepwise redox reaction steps of lithium polysulfides. Although many studies assign the observed reduction peaks in symmetric

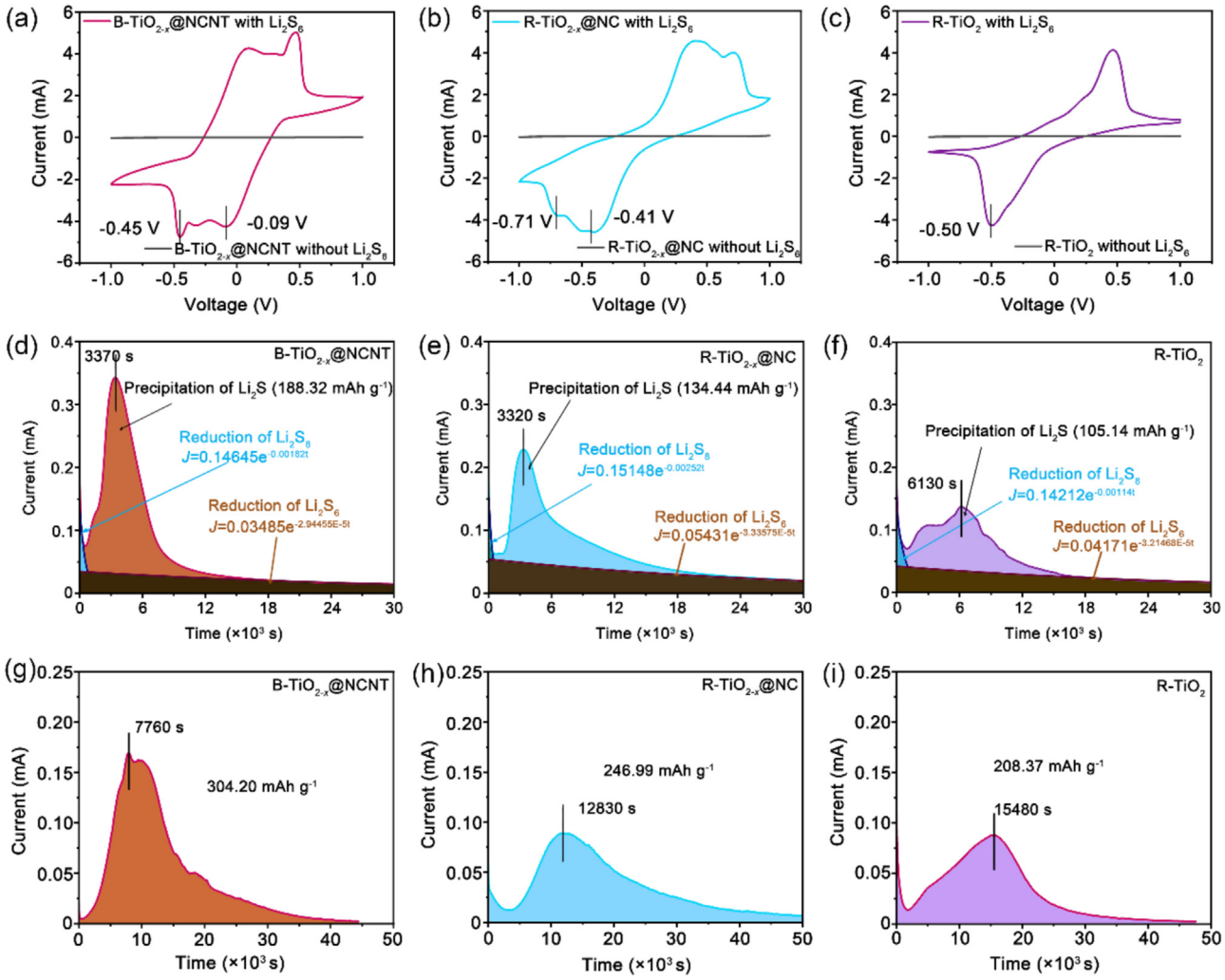

Fig. 4. CV curves of symmetric cells with (a) B-TiO_{2-x}@NCNT, (b) R-TiO_{2-x}@NC, (c) R-TiO_2 electrode, respectively. Potentiostatic discharge profile at 2.05 V on (d) B-TiO_{2-x}@NCNT, (e) R-TiO_{2-x}@NC, and (f) R-TiO_2 electrode for evaluating the nucleation kinetics of Li_2S. Potentiostatic charge profile at 2.4 V on (g) B-TiO_{2-x}@NCNT, (h) R-TiO_{2-x}@NC, and (i) R-TiO_2 electrode for evaluating decomposition kinetics of Li_2S.

cells solely to the reduction reactions occurring on the working electrodes [52,53], it should be noted that the counter electrode simultaneously undergoes an oxidation process, and its polarization behavior also influences the overall recorded current response. However, these peaks exhibit the highest current density, the fastest current response, and the smallest potential polarization among all the tested electrodes. These advantages can be attributed to this well-designed B-TiO_{2-x}@NCNT, which offers enhanced conductivity, stronger adsorption toward polysulfides, and better catalytic activity, thereby significantly facilitating the conversion of polysulfides. In contrast, for the R-TiO_{2-x}@NC electrode, two reduction peaks appear at −0.41 and −0.71 V (Fig. 4b), while only one peak is present at −0.50 V for the R-TiO_2 electrode (Fig. 4c). The lower current intensity and larger peak separation of the latter two indicate higher polarization and slower redox kinetics.

Throughout the discharge process of Li-S batteries, namely the reduction of sulfur, the reaction barrier is the highest during the nucleation process from liquid polysulfides to solid Li_2S_2/Li_2S. In particular, the conversion from Li_2S_2 to Li_2S is confirmed as the rate-limiting step [54,55]. Since the reduction from Li_2S_4 to Li_2S contributes to 75% of the theoretical capacity, improving the nucleation efficiency of Li_2S is essential for increasing the energy output of Li-S batteries. The Li_2S precipitation experiments were performed to evaluate the electrocatalytic effect of B-TiO_{2-x}@NCNT, R-TiO_{2-x}@NC, and R-TiO_2 (Fig. 4d–f). At a constant potential of 2.06 V, the current density gradually drops, corresponding to the reduction of Li_2S_8 to Li_2S_6, then to Li_2S_4 [56]. Subsequently, when the voltage is adjusted to 2.05 V, the lower potential overcomes the energy barrier of Li_2S nucleation, leading to the current density increasing until reaching a peak. The time required to reach the peak current density reflects the response speed of Li_2S nucleation. It takes 6130 s to reach the current peak on the R-TiO_2 electrode. In contrast, the peak current is located at 3370 s of B-TiO_{2-x}@NCNT, which is similar to 3320 s of R-TiO_{2-x}@NC, suggesting the faster Li_2S nucleation. This comparison highlights that the oxygen vacancies present in B-TiO_{2-x}@NCNT and R-TiO_{2-x}@NC promote the nucleation process of Li_2S. As the insulation of Li_2S accumulates and the concentration of polysulfides decreases, the current density drops again until below 0.01 mA. Integration of the discharge curves determines that, under the same amount of Li_2S_8 addition, the precipitation capacity of Li_2S on the B-TiO_{2-x}@NCNT is 188.32 mAh g^{-1}, which is higher than 133.44 mAh g^{-1} on the R-TiO_{2-x}@NC and much higher than 105.14 mAh g^{-1} on the R-TiO_2. The adsorption of polysulfides occurs on the surface of TiO_2, while the nucleation of Li_2S requires a highly conductive substrate [21]. The NCNTs grown in situ via chemical vapor deposition (CVD) are tightly contacted with TiO_2, facilitating the adsorbed polysulfides on TiO_2 to nucleate rapidly. Additionally, the distribution of NCNTs both inside and outside of the hollow TiO_2 provides more pathways for the diffusion of polysulfides. These results and insights indicate the superb catalytic effect of B-TiO_{2-x}@NCNT on the nucleation and growth of Li_2S.

The charging process of Li-S batteries is the reverse process, in other words, it corresponds to the oxidation of Li_2S. However, due to the intrinsic insulating nature of Li_2S and the strong Li–S bonds in its antifluorite structure, the oxidation process of Li_2S requires a large energy to overcome the decomposition barrier [57]. Failure to completely oxidize Li_2S results in low Coulombic efficiency and leads to the accumulation of Li_2S, which increases the internal resistance of Li-S batteries and leads to a short span-life. Therefore, it is important to evaluate the decomposition of Li_2S on different sulfur hosts. Therefore, the Li_2S decomposition tests were performed with B-TiO_{2-x}@NCNT, R-TiO_{2-x}@NC, and R-TiO_2 electrodes (Fig. 4g–i). Based on the integration of current curves during constant charging at 2.4 V, the decomposition capacity on B-TiO_{2-x}@NCNT is 304.20 mAh g^{-1}, which is higher than 246.99 mAh g^{-1} on R-TiO_{2-x}@NC and 208.37 mAh g^{-1} on R-TiO_2. What is more, the peak current is reached in just 7760 s on B-TiO_{2-x}@NCNT, which is significantly less than 12830 s on R-TiO_{2-x}@NC and 15480 s on R-TiO_2. These results demonstrate that the synergistic effect of enhanced adsorption, superior catalytic activity, and high conductivity in B-TiO_{2-x}@NCNT can also facilitate the decomposition of Li_2S, which is crucial for improving the redox reversibility, Coulombic efficiency, and cycling stability of Li-S batteries.

Li-S batteries were assembled with B-TiO_{2-x}@NCNT/S, R-TiO_{2-x}@NC/S, and R-TiO_2/S as a cathode to evaluate their electrochemical performance. Electrochemical impedance spectroscopy (EIS) measurements were first performed on fresh cells as shown in Fig. S7. The diameter of the semicircle in low-frequency regions represents the charge transfer resistance (R_{ct}). It is evident that the B-TiO_{2-x}@NCNT/S possesses the lowest R_{ct}, which is mainly attributed to the high conductive NCNTs. Fig. 5(a) and Fig. S8 show the typical CV curves as the scan rate gradually increases from 0.1 to 0.6 mV s^{-1}. Taking B-TiO_{2-x}@NCNT/S at 0.1 mV s^{-1} as an example, two reduction peaks A and B appear in the negative scan at 2.31 and 2.05 V, corresponding to the reduction from sulfur to long-chain polysulfides and further reduction to Li_2S_2/Li_2S, respectively. In the subsequent positive scan, the peaks C and D are located at 2.31 and 2.38 V, corresponding to the opposite oxidation process from Li_2S_2/Li_2S to short-chain lithium polysulfides and then to long-chain species or sulfur. With the increase in scan rate, the current response of all cathodes increases accordingly, indicating typical diffusion-controlled electrochemical behavior. At the scan rate of 0.6 mV s^{-1}, the CV curves of B-TiO_{2-x}@NCNT/S still remain sharp with well-defined redox peaks and a steadily increasing current density, indicating that the electrochemical reactions of sulfur species are rapid and efficient. In contrast, the CV curves of R-TiO_{2-x}@NC/S and R-TiO_2/S exhibit distortion and larger voltage hysteresis to some extent (Fig. S8a, c). Meanwhile, the redox peak voltages gradually shift, the reduction peaks move to lower potential, and the oxidation peaks shift to higher potential (Fig. S9a, b). The reduction peak B and oxidation peak C correspond to the liquid-solid and solid-liquid conversion processes of Li-S batteries during discharge and charge, respectively. The potential difference (ΔEp) between peaks B and C is used to reflect the redox polarization. As shown in Fig. S9(c and d), B-TiO_{2-x}@NCNT/S always represents smaller ΔEp across increasing scan rates, confirming its superior electrochemical reversibility and lower polarization.

What is more, there is a good linear relationship observed between the peak current density and the square root of the scan rate (Fig. 5b). The lithium diffusion coefficient can be evaluated by the Randles-Sevcik equation.

$$I_p = \left(2.69 \times 10^5\right) n^{1.5} A D_{Li}^{0.5} v^{0.5} C_{Li}$$

where I_p is the peak current density, n is the number of electrons transferred in this electrochemical process, A is the electrode area, D_{Li} is the lithium-ion diffusion coefficient, v is the scan rate, and C_{Li} is the molar concentration of lithium-ions. The slope of I_p-$v^{0.5}$ can reflect the efficiency of lithium-ion diffusion. As shown in Fig. 5(b) and Fig. S8(b and d), the slopes of B-TiO_{2-x}@NCNT/S are −4.29, −6.05, 9.82, and 10.04 for peak currents A, B, C, and D, respectively. These slopes are significantly higher than those of R-TiO_{2-x}@NC/S and R-TiO_2/S cathodes, which reflects that the sulfur redox reaction on B-TiO_{2-x}@NCNT has better reaction kinetics.

Fig. 5(c) and Fig. S10 depict the discharge-charge profiles of B-TiO_{2-x}@NCNT/S, R-TiO_{2-x}@NC/S, and R-TiO_2/S under the current densities of 0.2 and 5 C. The discharge curve of B-TiO_{2-x}@NCNT/S shows two plateaus at ~2.3 and ~2.1 V, corresponding to the multi-step reduction from S to Li_2S, which is consistent with CV curves. During charging, there is only one obvious long plateau at ~2.3 V due to the decomposition of

Li_2S requiring a large overpotential. The potential difference between charging and discharging is denoted as ΔV. The cathode B-TiO_{2-x}@NCNT/S exhibits the smallest ΔV at 0.2 C, while R-TiO_2/S shows significantly larger polarization. This difference is more pronounced at a high current density of 5 C (Fig. S10), where R-TiO_2/S can no longer reach the discharge plateau. By contrast, although the ΔV for B-TiO_{2-x}@NCNT/S also increases a lot, it still maintains clear and smooth discharge-charge plateaus, which demonstrates that the electrochemical redox reactions of sulfur species are easier to take place on B-TiO_{2-x}@NCNT. As a result, the fast sulfur reaction kinetics enable B-TiO_{2-x}@NCNT/S to achieve outstanding rate performance (Fig. 5d). At current densities of 0.2, 0.5, 1, 2, 3, 4, and 5 C, B-TiO_{2-x}@NCNT/S delivers the specific capacity of 1234.3, 998.3, 849.3, 744.0, 685.4, 634.9, and 589.2 mAh g^{-1} (average of 5 cycles), far exceeding R-TiO_{2-x}@NC/S and R-TiO_2/S particularly at high current density of 5 C of 388.1 and 127.6 mAh g^{-1}, respectively. Additionally, the comparison of cycling performance was investigated at 0.2 C as shown in Fig. 5(e). After 100 cycles, B-TiO_{2-x}@NCNT/S retains a capacity of 1034.6 mAh g^{-1}, corresponding to high-capacity retention of 83.7%, which is also much higher than that of R-TiO_{2-x}@NC/S (776.2 mAh g^{-1} with 69.5% retention) and R-TiO_2/S (515.1 mAh g^{-1} with 49.1% retention). Long-cycling measurement at high current density is crucial for evaluating the lifespan and stability of Li-S batteries. As illustrated in Fig. 5(f), R-TiO_{2-x}@NC/S maintains only 121.4 mAh g^{-1} after 1000 cycles at 5 C. In contrast, B-TiO_{2-x}@NCNT/S exhibits a specific capacity of 559.1 mAh g^{-1} at the first cycle, which increases to 636.0 mAh g^{-1} at the second cycle due to the activation process of the cathode at high current density. By the 1000th cycle, B-TiO_{2-x}@NCNT/S retains a specific capacity of 434.7 mAh g^{-1}, which corresponds to a retention of 68.3% with a capacity decay rate as low as 0.035% per cycle (calculated from the 2nd cycle). The average Coulombic efficiency of 1000 cycles is 98.9%, demonstrating excellent reversibility and long-cycling stability.

Notably, high sulfur loading remains a significant challenge for the commercial application of Li-S batteries. In addition, lean electrolyte addition is also considered another crucial factor for high-energy-density Li-S batteries. Therefore, the cycling performance of this well-designed B-TiO_{2-x}@NCNT/S was further explored with a high sulfur loading of 5.6 mg cm^{-2} and low electrolyte addition of 9.1 μL mg^{-1}. As shown in Fig. 5(g), the first discharge areal capacity is 4.48 mAh cm^{-2} at 0.2 C, which corresponds to a gravimetric capacity of 802.6 mAh g^{-1}. After 200 cycles, the areal capacity is 3.54 mAh cm^{-2} and the gravimetric capacity is 634.0 mAh g^{-1},

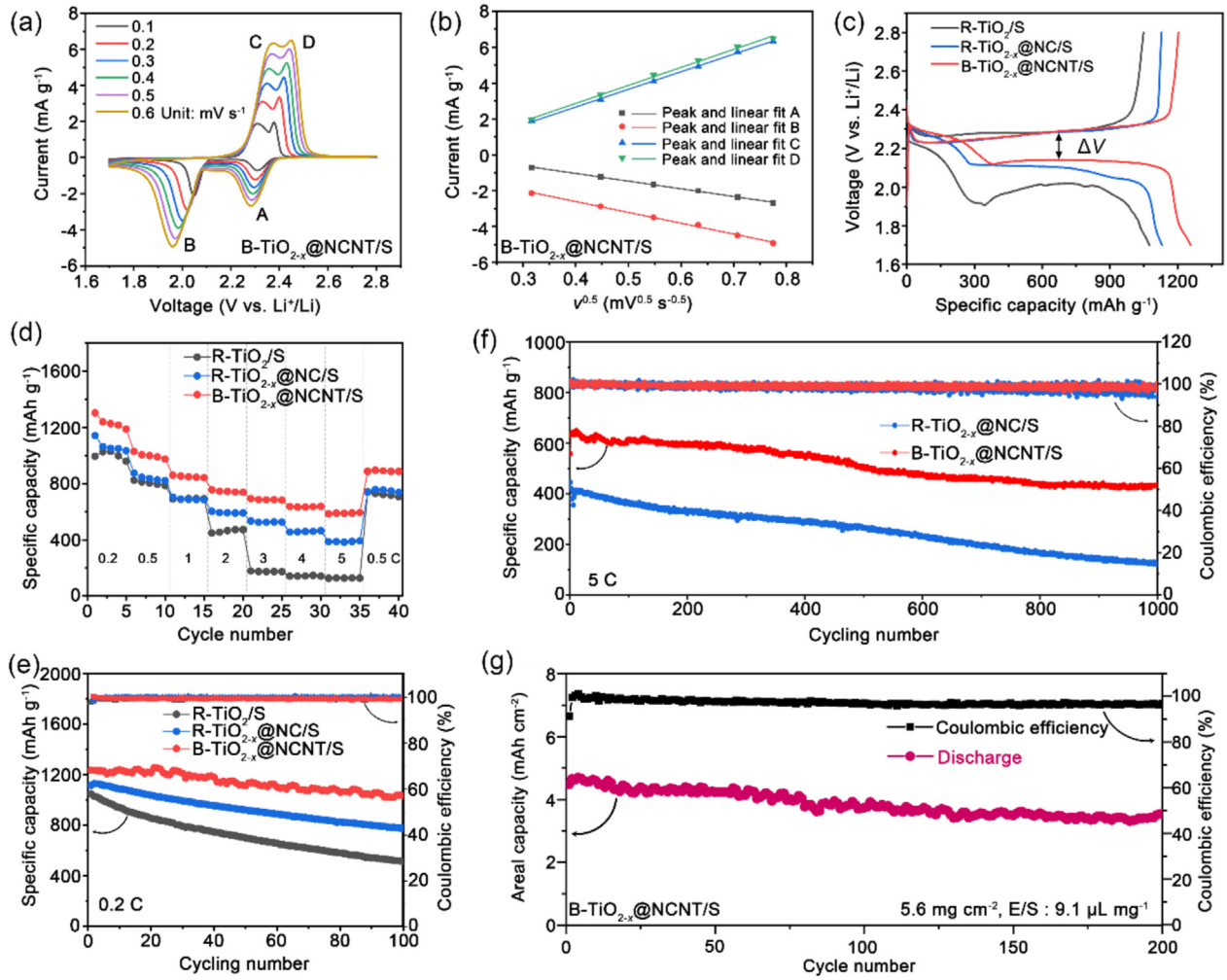

Fig. 5. (a) CV profiles at different scan rates of B-TiO_{2-x}@NCNT/S cathode and (b) corresponding I-$v^{0.5}$ linear fitting curves. (c) Discharge and charge profiles at 0.2 C of R-TiO_2/S, R-TiO_{2-x}@NC/S, and B-TiO_{2-x}@NCNT/S. (d) Rate performance of R-TiO_2/S, R-TiO_{2-x}@NC/S, and B-TiO_{2-x}@NCNT/S at 0.2, 0.5, 1, 2, 3, 4, 5, and 0.5 C. (e) Cycling performance of R-TiO_2/S, R-TiO_{2-x}@NC/S, and B-TiO_{2-x}@NCNT/S at 0.2 C. (f) Long cycling performance of R-TiO_{2-x}@NC/S and B-TiO_{2-x}@NCNT/S at 5 C. (g) High sulfur loading test: cycling performance of B-TiO_{2-x}@NCNT/S at 0.2 C under 5.6 mg cm^{-2} sulfur loading and electrolyte/sulfur ratio of 9.1 μL mg^{-1}.

indicating a capacity retention of 79.0%. These results highlight the superiority of B-TiO_{2-x}@NCNT as sulfur-host material for advanced Li-S batteries.

3. Conclusions

A biphasic homojunction TiO_2 enriched with oxygen vacancies and decorated with nitrogen-doped carbon nanotubes (B-TiO_{2-x}@NCNT) was designed as a multifunctional sulfur host and achieved a smooth polysulfide adsorption-conversion process. DFT calculations and experimental results reveal that soluble polysulfides are first immobilized at the biphasic homojunction interface by enhanced binding energies. Subsequently, polysulfides rapidly convert and nucleate to Li_2S under the catalytic effect of abundant oxygen vacancies and high conductivity of NCNTs. Additionally, B-TiO_{2-x}@NCNT can also facilitate the decomposition of Li_2S, ensuring efficient bidirectional sulfur redox reactions. Moreover, a large number of NCNTs densely grown inside and outside of hollow TiO_2 promote fast electron transfer and increase the lithium-ion diffusion coefficient, thereby enhancing the electrochemical kinetics of the Li-S battery. Overall, the corresponding Li-S battery delivered a high specific capacity (1234.3 mAh g^{-1} at 0.2 C), superior fast charge-discharge ability (589.2 mAh g^{-1} at 5 C), and long cycling stability (1000 cycles at 5 C with a low decay rate of 0.035%). More promisingly, even at a high sulfur loading of 5.6 mg cm^{-2}, stable cycling with 79.0% retention after 200 cycles can be achieved at 0.2 C. This work demonstrates the concept that coupling a biphasic homojunction interface and oxygen vacancies in one metal oxide can simultaneously enhance both adsorption ability and catalytic activity toward polysulfides.

Experimental section

Experimental details can be found in the Supporting Information.

CRediT authorship contribution statement

Hao Wang: Writing – original draft, Validation, Methodology, Investigation, Funding acquisition, Formal analysis, Data curation. **Shidi Huang:** Writing – review & editing, Methodology, Funding acquisition, Data curation. **Zhe Cui:** Writing – review & editing, Software, Formal analysis. **Jinqi Zhu:** Resources, Data curation. **Rujia Zou:** Writing – review & editing, Supervision, Project administration, Funding acquisition.

Declaration of competing interest

The authors declare that they have no known competing financial interests or personal relationships that could have appeared to influence the work reported in this paper.

Acknowledgments

This work was supported by the National Natural Science Foundation of China (Grant No.52372281), the Fundamental Research Funds for the Central Universities (2232020G-07), the foundation of Shanghai Institute of Technology (grant no. YJ2022-37), the Graduate Student Innovation Fund of Donghua University (CUSF-DH-D-2022007), the State Key Laboratory of Advanced Fiber Materials (KF2517), and the Program for Professor of Special Appointment (Eastern Scholar) at Shanghai Institutions of Higher Learning.

Appendix A. Supplementary material

Supplementary material to this article can be found online at https://doi.org/10.1016/j.jechem.2025.04.062.

References

[1] Z.N. Li, I. Sami, J.U. Yang, J.T. Li, R.V. Kumar, M. Chhowalla, Nat. Energy 8 (2023) 84–93.
[2] S.Y. Zhou, J. Shi, S.G. Liu, G. Li, F. Pei, Y.H. Chen, J.X. Deng, Q.Z. Zheng, J.Y. Li, C. Zhao, I. Hwang, C.J. Sun, Y.Z. Liu, Y. Deng, L. Huang, Y. Qiao, G.L. Xu, J.F. Chen, K. Amine, S.G. Sun, H.G. Liao, Nature 621 (2023) 75–81.
[3] X.Y. Li, S. Feng, C.X. Zhao, Q. Cheng, Z.X. Chen, S.Y. Sun, X. Chen, X.Q. Zhang, B.Q. Li, J.Q. Huang, Q. Zhang, J. Am. Chem. Soc. 144 (2022) 14638–14646.
[4] X.Y. Li, S. Feng, Y.W. Song, C.X. Zhao, Z. Li, Z.X. Chen, Q. Cheng, X. Chen, X.Q. Zhang, B.Q. Li, J.Q. Huang, Q. Zhang, Am. Chem. Soc. 146 (2024) 14754–14764.
[5] X.Y. Li, S. Feng, M. Zhao, C.X. Zhao, X. Chen, B.Q. Li, J.Q. Huang, Q. Zhang, Angew. Chem. Int. Edit. 61 (2022) e202114671.
[6] M.Y. Wang, Z.C. Bai, T. Yang, C.H. Nie, X. Xu, Y.X. Wang, J. Yang, S.X. Dou, N.N. Wang, Adv. Energy Mater. 12 (2022) 2201585.
[7] Z.Y. Han, R.H. Gao, Y.Y. Jia, M.T. Zhang, Z.J. Lao, B.A. Chen, Q. Zhang, C. Li, W. Lv, G.M. Zhou, Mater. Today 57 (2022) 84–120.
[8] X.L. Ji, K.T. Lee, L.F. Nazar, Nat. Mater. 8 (2009) 500–506.
[9] L.T. Ren, J. Liu, Y.J. Zhao, Y. Wang, X.W. Lu, M.Y. Zhou, G.X. Zhang, W. Liu, H.J. Xu, X.M. Sun, Adv. Funct. Mater. 33 (2023) 2210509.
[10] M.P. Yu, J.S. Ma, H.Q. Song, A.J. Wang, F.Y. Tian, Y.S. Wang, H. Qiu, R.M. Wang, Energy Environ. Sci. 9 (2016) 1495–1503.
[11] P. Feng, K. Dong, Y.L. Xu, X. Zhang, H.J. Jia, H. Prell, M. Tovar, I. Manke, F.Y. Liu, H.X. Xiang, M.F. Zhu, Y. Lu, Adv. Fiber Mater. 6 (2024) 810–824.
[12] K.Z. Cao, H.Q. Liu, Y. Li, Y.J. Wang, L.F. Jiao, Energy Storage Mater. 9 (2017) 78–84.
[13] D.S. Wu, F.F. Shi, G.M. Zhou, C.X. Zu, C. Liu, K. Liu, Y.Y. Liu, J.Y. Wang, Y.C. Peng, Y. Cui, Energy Storage Mater. 13 (2018) 241–246.
[14] E.S. Sim, G.S. Yi, M.Y. Je, Y.B. Lee, Y.C. Chung, J. Power Sources 342 (2017) 64–69.
[15] Y. Wang, R. Zhang, J. Chen, H. Wu, S. Lu, K. Wang, H. Li, C.J. Harris, K. Xi, R.V. Kumar, S. Ding, Adv. Energy Mater. 9 (2019) 1900953.
[16] Z. Li, C. Zhou, J. Hua, X. Hong, C. Sun, H.-W. Li, X. Xu, L. Mai, Adv. Mater. 32 (2020) 1907444.
[17] M.D. Zhang, J.W. Mu, Y.N. Li, Y.Y. Pan, Z.L. Dong, B. Chen, S.W. Guo, W.H. Yuan, H.Q. Fang, H. Hu, M.B. Wu, J. Energy Chem. 78 (2023) 105–114.
[18] T. Ren, X.J. Dong, X.L. Li, H.J. Zhu, C. Yang, J.L. Zhu, J. Energy Chem. 101 (2025) 837–843.
[19] B.Y. Li, Q.M. Su, L.T. Yu, J. Zhang, G.H. Du, D. Wang, D. Han, M. Zhang, S.K. Ding, B.S. Xu, ACS Nano 14 (2020) 17285–17294.
[20] J. Wu, T. Ye, Y.C. Wang, P.Y. Yang, Q.C. Wang, W.Y. Kuang, X.L. Chen, G.H. Duan, L.M. Yu, Z.Q. Jin, J.Q. Qin, Y.P. Lei, ACS Nano 16 (2022) 15734–15759.
[21] T. Zhou, W. Lv, J. Li, G. Zhou, Y. Zhao, S. Fan, B. Liu, B. Li, F. Kang, Q.H. Yang, Energy Environ. Sci. 10 (2017) 1694–1703.
[22] L. Jiao, C. Zhang, C. Geng, S. Wu, H. Li, W. Lv, Y. Tao, Z. Chen, G. Zhou, J. Li, G. Ling, Y. Wan, Q.H. Yang, Adv. Energy Mater. 9 (2019) 1900219.
[23] L. Ma, Y.Q. Zhang, S. Zhang, L. Wang, C.X. Zhang, Y.J. Chen, Q. Wu, L.B. Chen, L.J. Zhou, W.F. Wei, Adv. Funct. Mater. 33 (2023) 2305788.
[24] M. Xiong, W.J. Zou, K. Fan, C.C. Qin, S.B. Li, L.F. Fei, J.Z. Jiang, H.T. Huang, L. Shen, F. Gao, A.K.Y. Jen, K. Yao, ACS Energy Lett. 7 (2022) 550–559.
[25] C. Ma, Y.Q. Zhang, Y.M. Feng, N. Wang, L.J. Zhou, C.P. Liang, L.B. Chen, Y.Q. Lai, X.B. Ji, C.L. Yan, W.F. Wei, Adv. Mater. 33 (2021) 2100171.
[26] L. Ren, Y.Z. Li, M.Y. Mao, L. Lan, X.B. Lao, X.J. Zhao, Appl. Surf. Sci. 490 (2019) 283–292.
[27] X.Q. Huang, R.K. Zhang, X.R. Gao, B.R. Yu, Y.Z. Gao, Z.G. Han, Int. J. Hydrog. Energy 46 (2021) 26358–26366.
[28] F. Yang, X. Wang, D.Q. Zhang, J. Yang, D. Luo, Z.W. Xu, J.K. Wei, J.Q. Wang, Z. Xu, F. Peng, X.M. Li, R.M. Li, Y.L. Li, M.H. Li, X.D. Bai, F. Ding, Y. Li, Nature 510 (2014) 522–524.
[29] X. Tang, W.Y. Chu, J.S. Qian, J.C. Lin, G.Z. Cao, Small 13 (2017) 1701964.
[30] Y.X. Hu, Y.Y. Pan, Z.L. Wang, T.G. Lin, Y.Y. Gao, B. Luo, H. Hu, F.T. Fan, G. Liu, L.Z. Wang, Nat. Commun. 11 (2020) 2129.
[31] J. Lee, C. Choi, J.B. Park, S. Yu, J. Ha, H. Lee, G. Jang, Y.S. Park, J. Yun, H. Im, S. Moon, S. Lee, J.I. Choi, D.W. Kim, J. Moon, J. Energy Chem. 83 (2023) 496–508.
[32] Y. Li, K.A. Min, B. Han, L.Y.S. Lee, Appl. Catal. B 282 (2021) 119548.
[33] K. Katsiev, G. Harrison, H. Alghamdi, Y. Alsalik, A. Wilson, G. Thornton, H. Idriss, J. Phys. Chem. C 121 (2017) 2940–2950.
[34] Y. Wang, H.J. Sun, S.J. Tan, H. Feng, Z.W. Cheng, J. Zhao, A.D. Zhao, B. Wang, Y. Luo, J.L. Yang, J.G. Hou, Nat. Commun. 4 (2013) 2214.
[35] R. Katal, S. Masudy-Panah, M. Tanhaei, M. Farahani, J.Y. Hu, Chem. Eng. J. 384 (2020) 123384.
[36] Z.D. Yu, S.H. Xun, M.Z. Jing, H.F. Chen, W.Y. Song, Y.H. Chao, M. Rahmani, Y.X. Ding, M.Q. Hua, J. Liu, W.S. Zhu, J. Hazard. Mater. 440 (2022) 129859.
[37] H.B. Yin, Z.T. Pu, J.W. Xue, P.Y. Ma, B. Wu, M. Han, H.F. Lin, Z.T. Luo, J. Zeng, X.L. Ma, H.L. Li, ACS Catal. 13 (2023) 7608–7615.
[38] B.K. Zhang, D.B. Wang, S.J. Jiao, Z.K. Xu, Y.X. Liu, C.C. Zhao, J.W. Pan, D.H. Liu, G. Liu, B.J. Jiang, Y.F. Li, L.C. Zhao, J.Z. Wang, Chem. Eng. J. 446 (2022) 137138.
[39] M. Huang, Y. Chu, B. Xi, N. Shi, B. Duan, C. Zhang, W. Chen, J. Feng, S. Xiong, Small 16 (2020) 2004054.

[40] Y. Lu, Y.X. Liu, L. He, L.Y. Wang, X.L. Liu, J.W. Liu, Y.Z. Li, G. Tian, H. Zhao, X.H. Yang, J. Liu, C. Janiak, S. Lenaerts, X.Y. Yang, B.L. Su, Nanoscale 12 (2020) 8364–8370.
[41] M. Ni, D. Sun, X. Zhu, Q. Xia, Y. Zhao, L. Xue, J. Wu, C. Qiu, Q. Guo, Z. Shi, X. Liu, G. Wang, H. Xia, Small 16 (2020) 2006366.
[42] A.B. Fuertes, G.A. Ferrero, M. Sevilla, J. Mater. Chem. A 2 (2014) 14439–14448.
[43] Y. Dai, W. Zheng, X. Li, A. Liu, W. Zhang, X. Jiang, X. Wu, J. Tao, G. He, ACS Appl. Mater. Interfaces 13 (2021) 2521–2529.
[44] X. Li, X.L. Sun, Front. Energy Res. 2 (2014) 49.
[45] Y. Fang, Y. Zhang, C. Miao, K. Zhu, Y. Chen, F. Du, J. Yin, K. Ye, K. Cheng, J. Yan, G. Wang, D. Cao, Nano-Micro Lett. 12 (2020) 128.
[46] X. Bi, G.H. Du, A. Kalam, D.F. Sun, Y. Yu, Q.M. Su, B.S. Xu, A.G. Al-Sehemi, Chem. Eng. Sci. 234 (2021) 116440.
[47] Q. Ni, R. Dong, Y. Bai, Z. Wang, H. Ren, S. Sean, F. Wu, H. Xu, C. Wu, Energy Storage Mater. 25 (2020) 903–911.
[48] M. Setvín, U. Aschauer, P. Scheiber, Y.F. Li, W.Y. Hou, M. Schmid, A. Selloni, U. Diebold, Science 341 (2013) 988–991.
[49] Z. Futera, N.J. English, J. Phys. Chem. C 121 (2017) 6701–6711.
[50] N.R. Li, L.H. Yu, J.Y. Yang, B.B. Zheng, X.P. Qiu, J.Y. Xi, Nano Energy 79 (2021) 105466.
[51] R. Wang, J.L. Yang, X. Chen, Y. Zhao, W.G. Zhao, G.Y. Qian, S.N. Li, Y.G. Xiao, H. Chen, Y.S. Ye, G.M. Zhou, F. Pan, Adv. Energy Mater. 10 (2020) 1903550.
[52] Y. Liu, A. Chatterjee, P. Rusch, C. Wu, P. Nan, M. Peng, F. Bettels, T. Li, C. Ma, C. Zhang, B. Ge, N.C. Bigall, H. Pfnuer, F. Ding, L. Zhang, ACS Nano 15 (2021) 15047–15056.
[53] C.X. Dong, C.N. Ma, C. Zhou, Y.K. Yu, J.J. Wang, K.S. Yu, C.L. Shen, J.P. Gu, K.J. Yan, A. Zheng, M.J. Gong, X. Xu, L.Q. Mai, Adv. Mater. 36 (2024) 2407070.
[54] H. Wang, Z. Cui, S.A. He, J.Q. Zhu, W. Luo, Q. Liu, R.J. Zou, Nano-Micro Lett. 14 (2022) 189.
[55] H. Gao, Y.F. Zhang, M.L. Wang, R.X. Yang, S. Feng, X. Cao, Y.P. Zhang, Z.Y. Lu, Y.Z. Song, J. Energy Chem. 100 (2025) 192–200.
[56] F.Y. Fan, W.C. Carter, Y.-M. Chiang, Adv. Mater. 27 (2015) 5203–5209.
[57] Y. Guo, H.C. Jin, Z.K. Qi, Z.Q. Hu, H.X. Ji, L.J. Wan, Adv. Funct. Mater. 29 (2019) 1807676.